A physics-based high-resolution BIPV model for building performance simulations

Juliana E. Goncalves[a,b,*], Twan van Hooff[a,c], Dirk Saelens[a,b]

[a]*Department of Civil Engineering, Building Physics Section, KU Leuven, Leuven, Belgium*
[b]*EnergyVille, Genk, Belgium*
[c]*Department of the Built Environment, unit Building Physics and Services, Eindhoven University of Technology, Eindhoven, The Netherlands*

Abstract

Building integrated photovoltaic (BIPV) systems are considered a promising solution to increase the share of renewable energy in the built environment. To evaluate the BIPV performance at the building level, the implementation of BIPV models in building performance simulation tools is an essential step. This paper presents the development of a multi-physics BIPV model for the simulation of BIPV facades within the openIDEAS framework for building and district energy simulations. The model couples a high-resolution electrical model to physics-based thermal and airflow models. The combination of these two modelling approaches is not common in BIPV models, particularly for building performance simulations. The model predictions are compared to three months of experimental data from a naturally ventilated BIPV module installed in the facade of a test building in Leuven, Belgium. A good agreement is obtained in terms of both BIPV energy yield and temperature. The error in daily energy yield estimations is on average below 3 % and the error in the monthly energy yield is below 2 %. The back-of-module temperature is predicted with a MAE lower than 2 °C and RMSE lower than 5 °C.

Keywords: Building integrated photovoltaic (BIPV), Building performance simulation (BPS), Energy yield, Temperature, Natural ventilation
2010 MSC: 00-01, 99-00

*Corresponding author

1. Introduction

One of the main challenges concerning energy use and greenhouse gas emissions is the future sustainability of urban areas. Worldwide, nations have set strategic plans to promote the deployment of renewable energy and reduce the CO_2 emissions related to the built environment. In the European Union, the Energy Performance of Buildings Directive (Directive 2010/31/EU) states that all new buildings must be nearly zero-energy buildings (NZEB) by 2021 and supports, in parallel, the transformation of existing buildings into NZEBs (EPBD, 2010). In China, the government issued the China Act on the Energy Efficiency of Civil Buildings to promote energy efficiency and decrease the energy consumption in buildings (Ma et al., 2018). Equally important energy policies have been defined in Latin American countries, such as Argentina, Brazil, Chile and Uruguay (Silvero et al., 2018).

In addition to improving the energy efficiency of buildings, the deployment of renewable energy sources in the built environment is a key step towards the reduction of fossil fuels consumption in the building sector. Photovoltaic (PV) technology is particularly suitable as renewable energy source in view of its stable market increase and price reduction (Masson & Brunisholz, 2015). PV modules have usually been used in the built environment as open-rack installations on building roofs (Sánchez-Pantoja et al., 2018), which classify them as building applied photovoltaic (BAPV). BAPVs are not commonly employed on building facades, mainly due to aesthetic reasons (Aguacil et al., 2019).

Alternatively, the concept of building integrated photovoltaic (BIPV) concerns the use of PV elements as part of the building envelope. Besides generating electricity, BIPV modules perform at least one additional function, such as insulation, weather barrier or sun shading (Osseweijer et al., 2018). By replacing conventional building components, BIPVs provide savings in land, materials and construction time (Jelle et al., 2012). The assimilation of PV into the building architectural concept is also facilitated (Saretta et al., 2018; Aguacil et al., 2019). The prospect to exploit additional surfaces for renewable energy generation in the built environment makes BIPV a key technology to comply with the increasingly stricter building energy policies. In particular, facade integration is considered a promising BIPV application, complementing the limited roof surface area (Osseweijer et al., 2018). BIPV facades can also provide a balanced power generation profile over the day, with relatively higher energy production in the early and late daylight hours (Redweik et al., 2013; Brito et al., 2017; Díez-Mediavilla et al., 2019).

Over the recent years, a significant effort has been invested in the development of BIPV models, as reviewed by Norton et al. (2011), Agathokleous & Kalogirou (2016), Yang & Athienitis (2016) and Biyik et al. (2017). Concerning the level of detail of the BIPV models, two trends are observed. On the one hand, BIPV models that propose a detailed physics-based thermal modelling often employ a simplified electrical model, assuming that the PV efficiency decreases linearly with increasing operating temperature, e.g. Assoa & Ménézo (2014), Ioannidis et al. (2017) Athienitis et al. (2018), Assoa et al. (2018), Ghosh et al. (2019), Alrashidi et al. (2020). On the other hand, BIPV models that propose a high-resolution electrical model either employ a simplified thermal model, e.g. Tsai (2010), d'Alessandro et al. (2015), Hofer et al. (2016), Sprenger et al. (2016), Gallardo-Saavedra & Karlsson (2018) and Walker et al. (2019), and/or focus on stand alone PV modules, e.g. Tsai (2010), d'Alessandro et al. (2015), Goverde et al. (2017) and Horváth et al. (2018). Moreover, most of high-resolution (BI)PV models are developed in software dedicated to the simulation of electrical circuits, such as PSPICE or LTSpice (e.g. Tsai (2010); d'Alessandro et al. (2015); Goverde et al. (2017); Horváth et al. (2018); Gallardo-Saavedra & Karlsson (2018)). Although such circuit-based environments can be used to represent the thermal behaviour of PV modules, they are not particularly suitable for building performance simulations.

Another important aspect that deserves further attention is the influence of the wind flow on the heat dissipation conditions in BIPV elements. As research on wind flow in the built environment progresses, new insights on how the wind affects the convective heat dissipation in buildings have been published (Emmel et al., 2007; Defraeye et al., 2011; Mirsadeghi et al., 2013; Montazeri et al., 2015; Montazeri & Blocken, 2017, 2018; Iousef et al., 2019). In particular, it has been demonstrated that convective heat transfer coefficients resulting from wind effects not only vary over the building surfaces, but also depend on the building geometry (Montazeri et al., 2015; Montazeri & Blocken, 2017). However, BIPV models are often based on simplified models for the exterior convective heat transfer that only take the wind speed into account in a linear relationship, e.g. Assoa & Ménézo (2014) Buonomano et al. (2016)Athienitis et al. (2018) Assoa et al. (2018) Alrashidi et al. (2020). A further simplification is the use of a constant value for the convective heat transfer coefficient as considered by Hu et al. (2017). This means that other important factors that influence the wind flow around a building, such as the wind direction, the building surroundings or the building surface (i.e. roof vs. facade surfaces), are not considered.

This paper proposes a multi-physics BIPV model for the simulation of BIPV facades within a building performance simulation (BPS) environment. The model combines a high-resolution electrical modelling with a detailed physics-based thermal and airflow modelling, which is not common in BIPV modelling. The multi-physics BIPV model predictions are compared to experimental data from a naturally ventilated crystalline silicon (c-Si) BIPV module. The comparison is based on energy yield and temperature results. Simplified BIPV power and temperature models available in the literature are also included in the comparative analysis. The relevance and novelty of this work lies on the combination of four aspects, discussed next.

First, the multi-physics BIPV model is developed as an exterior wall component within IDEAS library, an open-source Modelica-based library for building performance simulations (BPS). Incorporating a BIPV model as a wall component into IDEAS enables the simulation of the whole building, considering the thermal coupling between the BIPV element and building interior. The importance of this BIPV-building coupling has been discussed by Athienitis et al. (2018). In contrast to circuit-based modelling environments, the multidomain nature of Modelica language enables the combination of high-resolution (circuit-based) electrical models with thermal and airflow models within the same modelling platform (avoiding the need for co-simulation or decoupled simulation).

Second, the multi-physics BIPV model represents an improvement over BIPV models available for building performance simulation, in particular concerning the high-resolution electrical modelling. The PV electrical modelling employed in building simulations is generally based on power models, e.g. (Miyazaki et al., 2005; Didoné & Wagner, 2013; Ng et al., 2013; Ioannidis et al., 2017; Athienitis et al., 2018; Sánchez-Palencia et al., 2019), which represent a simplified approach with specific limitations (Roberts et al., 2017). In addition, BPS tools typically assume that all (BI)PV modules within the array operate at maximum power point (MPP) and under the same conditions. This means that mismatch losses are not taken into account and, therefore, neither shading (intra-array) nor different electrical architectures can be simulated.

Third, the multi-physics BIPV model is based on detailed physics-based thermal and airflow models. A physics-based modelling provides the flexibility necessary to carry out modifications of the BIPV design, which is not possible when (semi-)empirical temperature models are employed, e.g. Walker et al. (2019) and Gallardo-Saavedra & Karlsson (2018). Furthermore, compared to existing BIPV models in the literature, the multi-physics BIPV model considers the following three additional factors in the exterior convective heat transfer modelling: the building geometry, the wind direction, and the building surface (i.e. roof, windward, leeward or side facades). Another differentiation is that the airflow modelling in this paper is based on the experimental pressure characterisation of the BIPV module. Such experiments are not always carried out in BIPV studies; instead, a theoretical approach is normally employed, e.g. Ioannidis et al. (2017).

Fourth, the multi-physics BIPV model predictions are compared to experimental data from a naturally ventilated BIPV module that is fully integrated into a test building. The full building integration guarantees realistic boundary conditions for the BIPV operation (including realistic wind flow around a building). Note that BIPV setups are not always part of a realistic building structure, e.g. Ioannidis et al. (2017), Assoa et al. (2018), Agathokleous & Kalogirou (2018a), Agathokleous & Kalogirou (2018b), Walker et al. (2019) and Alrashidi et al. (2020). The comparative analysis also considers power predictions based on the linear power model and back-of-module temperature predictions based on (semi-)empirical correlations presented in the literature (Ross, 1976; Skoplaki et al., 2008; Skoplaki & Palyvos, 2009). The intention here is to assess possible differences between the results obtained from the multi-physics BIPV model and the results from these simplified models for the naturally ventilated BIPV module investigated in this paper.

This paper is structured as follows. The methodology is described in Section 2, starting with a general description of the BIPV module and the test building in Section 2.1. Next, Section 2.2 presents the multi-physics BIPV model in detail, covering thermal, airflow and electrical aspects. Section 2.3 describes the experimental setup used to monitor the weather conditions and the BIPV behaviour (power, temperature and heat flux measurements). Section 2.4 summarises the inputs used in the multi-physics BIPV model, including the experimental pressure characterisation. Section 3 presents the results of the comparative analysis between the experimental data, the multi-physics BIPV model, and the simplified models. Section 4 discusses the results and the limitations of the proposed multi-physics model, indicating the topics of ongoing and future research. Finally, the Section 5 concludes the paper.

2. Methodology

2.1. BIPV module and building description

A schematic representation of the naturally-ventilated BIPV module is presented in Figure 1. The BIPV module is composed of two PV mini-modules connected to a 14 cm cavity and a 15 cm Rockwool layer. Two openings of 0.58 x 0.05 m^2, one at the bottom and one at the top, allow the exterior air to flow

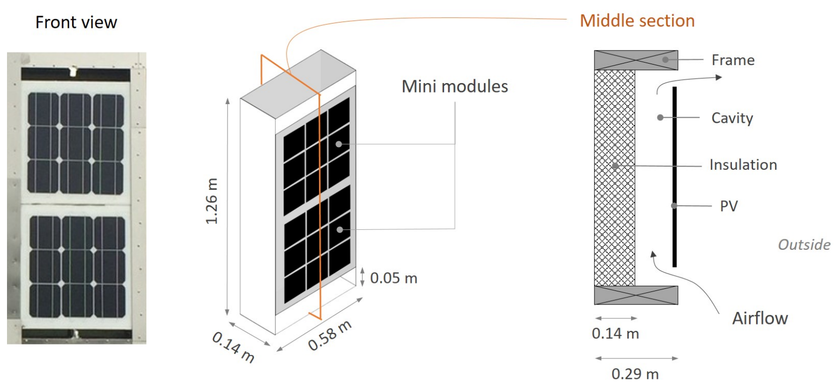

Figure 1: Front view and schematic representation of the BIPV module.

through the cavity to improve the heat dissipation. Each mini-module consists of nine monocrystalline silicon (c-Si) PV cells connected in series. The cells are encapsulated in a transparent EVA (ethyl vinyl acetate) layer at the front and in a white EVA layer at the back; both sides are covered with glass. The mini-modules that compose the BIPV module have been rated under standard test conditions (STC). Together, their power output is 70.6 W.

As shown in Figure 2a, the BIPV module was installed in the southwest facade of the Vliet test building in Leuven, Belgium (50°52′N, 4°41′E), ensuring realistic indoor and outdoor conditions. The inclination of the facade is 90 ° and its azimuth angle is 225 ° (north as reference). Figure 2b shows that the building has a rectangular footprint and is located in an open environment, mostly free of shading events from the surroundings. The building facade where the BIPV module was installed is 4.3 m high and 25.2 m wide.

2.2. Multi-physics BIPV model

Figure 3 presents the control volume approach employed in the multi-physics BIPV model. A BIPV control volume corresponds to the dimensions of one PV cell and includes the following layers: glass, PV cell, glass, air volume, and building wall. EVA layers are not explicitly modelled due to their small thickness compared to the glass thickness. The PV cells are modelled explicitly

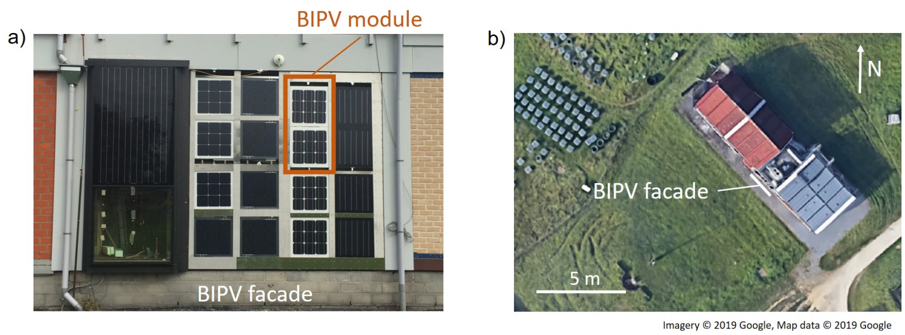

Figure 2: (a) The BIPV module integrated into the BIPV facade of the Vliet test building. (b) Surroundings of the Vliet test building (Google Maps image), indicating the BIPV southwest facade.

to enable the coupling between thermal and electrical model, which is achieved by using the PV cell to calculate the power output while imposing the generated power as a heat sink on the PV layer. The airflow through the cavity connects the BIPV control volume to one another.

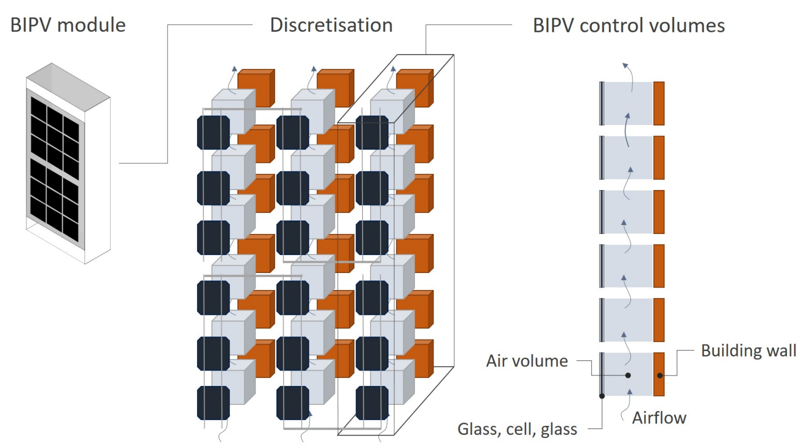

Figure 3: Control volume modelling approach applied to the ventilated BIPV module described in Section 2.1.

As illustrated in Figure 4, the multi-physics BIPV model was developed as an exterior wall component within IDEAS library, an open-source Modelica-based library for building performance simulations (BPS), part of the openIDEAS environment. IDEAS provides transient models for the simulation of thermal and electrical systems at both building and feeder level. IDEAS models have been verified against the IEA EBC BESTEST reference results and the IEA EBC Annex 58 Twin House experiments (Jorissen et al., 2018).

Figure 4 also illustrates the multi-physics structure of the BIPV model proposed in this paper, including electrical, thermal and airflow modelling. The couplings between electrical and thermal modelling, between thermal and airflow modelling as well as between the BIPV and the building zone are also indicated in this figure. The remainder of this section follows the same structure: the thermal modelling is described in Section 2.2.1, the airflow modelling in Section 2.2.2, and the electrical modelling in Section 2.2.3).

2.2.1. Thermal modelling

Figure 5 illustrates the different aspects of the thermal modelling that are encapsulated in one BIPV control volume. In a BIPV module, only part of the solar irradiance is converted into electricity by the PV cells. Another relatively small part is reflected by the glass surface. Most of the energy is dissipated as heat to the exterior environment and to the cavity, in the form of conductive, convective and radiative heat exchanges, described in detail here.

Conduction through the glass, PV cell and building wall is treated as a one-dimensional heat transfer problem, with conductive heat transfer computed as:

$$\mathrm{Q_{i,j}} = \mathrm{G_{ij}}\left(\mathrm{T_{i,j}} - \mathrm{T_{i,j+1}}\right)\mathrm{A} \tag{1}$$

with the time-derivative:

$$\mathrm{C_{i,j}}\frac{\mathrm{dT_{i,j}}}{\mathrm{dt}} = \left(\mathrm{Q_{i,j-1}} - \mathrm{Q_{i,j}}\right)\mathrm{A} \tag{2}$$

where each material layer i consists of $\mathrm{n_i}$ time-dependent temperature states $\mathrm{T_{ij}(t)}$ [K] with heat capacity $\mathrm{C_{i,j}}$ and $\mathrm{n_i}$-1 thermal conductors with thermal conductance $\mathrm{G_{i,j}}$. $\mathrm{C_{i,j}}$ and $\mathrm{G_{i,j}}$ are computed assuming homogeneous material thermal properties over each element layer. A is the surface area of a BIPV control volume.

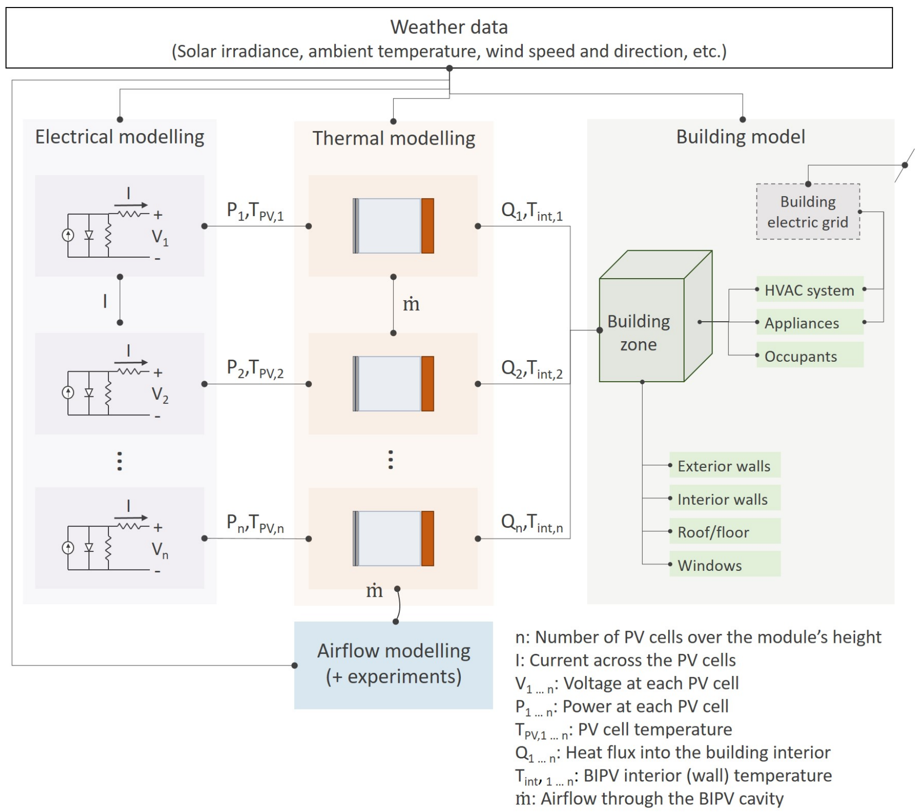

Figure 4: Multi-physics BIPV model composed of electrical, thermal and airflow modelling and integrated into the IDEAS environment.

As explained by Jorissen et al. (2018), the number of nodes n_i in each material layer is computed based on Wetter (2004), as follows:

$$n_i = \max\left(2, 3\frac{\Pi_i}{\Pi_{ref}}\right) \tag{3}$$

with

$$\Pi = \frac{d}{\sqrt{\alpha}} \tag{4}$$

where α is the thermal diffusivity of each layer i, and Π_{ref} is a reference value computed for a concrete slab of 20 cm.

For the PV layer, the PV power is included in Equation 2 as a heat sink (see

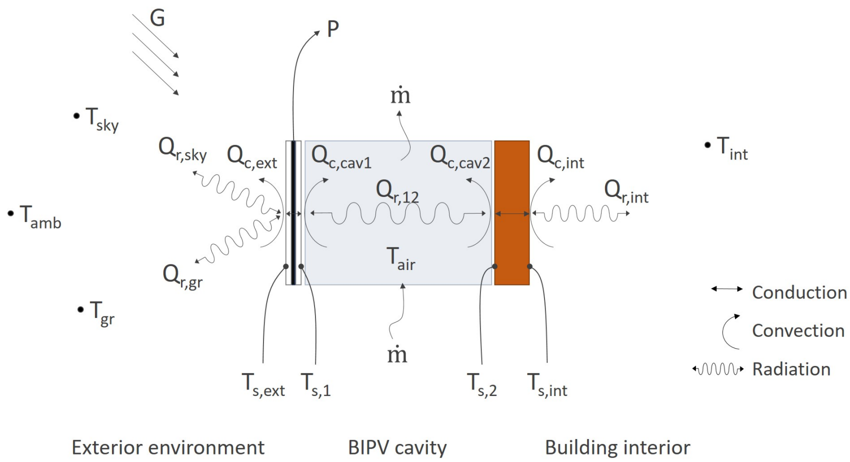

Figure 5: BIPV control volume, where G represents the solar irradiance, P represents the PV power as a heat sink, T [K] indicates temperatures at different locations, $\dot{m}$ represents the airflow through the cavity, and Q indicates heat exchanges.

Section 2.2.3 for the electrical modelling). Note that edge effects and vertical conduction between control volumes are not considered in the multi-physics BIPV model.

The heat exchange with the exterior environment is composed of radiative and convective heat exchanges, as follows:

$$Q_{ext} = Q_{r,sky} + Q_{r,gr} + Q_{c,ext} \tag{5}$$

where $Q_{r,sky}$ is the radiative heat transfer between the BIPV and the sky dome, $Q_{r,gr}$ is the radiative heat transfer between the BIPV and the ground, and $Q_{c,ext}$ is the convective heat transfer between the BIPV surface and the ambient air.

Assuming the sky dome and the ground as black bodies, $Q_{r,sky}$ and $Q_{r,sky}$ are defined as:

$$Q_{r,sky} = F_{sky} \varepsilon_{ext} \sigma \left(T_{s,ext}^4 - T_{sky}^4 \right) A \tag{6}$$

and

$$Q_{r,gr} = F_{gr} \varepsilon_{ext} \sigma \left(T_{s,ext}^4 - T_{gr}^4 \right) A \tag{7}$$

where $T_{s,ext}$ is the temperature of the exterior glass surface, T_{sky} is the effective sky temperature, T_{gr} is the ground temperature, F_{sky} is the view factor between the BIPV module and the sky, F_{gr} is the view factor between the BIPV module and the ground, ε_{ext} is the long-wave emissivity of the glass, σ is the Stefan-Boltzmann constant (= 5.67 x 10^{-8} W/m^2K^4), and A is the surface area of a BIPV control volume.

The view factors F_{sky} and F_{sky} are calculated as:

$$F_{sky} = \frac{1 + \cos\beta}{2} \tag{8}$$

and

$$F_{gr} = \frac{1 - \cos\beta}{2} \tag{9}$$

where β is the inclination of the surface (equal to 90 ° for BIPV facades).

In the multi-physics BIPV model, the ground surface temperature is assumed equal to the ambient temperature ($T_{gr} = T_{amb}$), and the sky temperature is based on the correlation proposed by Swinbank (1963):

$$T_{sky} = 0.0552 T_{amb}^{1.5} \tag{10}$$

The exterior convective heat transfer, $Q_{c,ext}$, is defined as:

$$Q_{c,ext} = h_{c,ext}\left(T_{s,ext} - T_{amb}\right)A \tag{11}$$

where $h_{c,ext}$ is the exterior convective heat transfer coefficient and T_{amb} is the ambient temperature.

To model $h_{c,ext}$, the multi-physics BIPV model combines natural and forced convection as follows (Bergman et al., 2011):

$$h_{c,ext} = \left(h_{c,f}^3 + h_{c,n}^3\right)^{\frac{1}{3}} \tag{12}$$

where $h_{c,f}$ is the forced convective heat transfer coefficient, and $h_{c,n}$ is the natural convective heat transfer coefficient. This formulation guarantees that natural convection dominates the heat transfer when forced convection is limited and vice-versa. This is important because forced and natural convection have significantly different magnitudes, with forced convection being stronger than natural convection, as highlighted by e.g. Agathokleous & Kalogirou (2016).

Forced convection is the result of the wind flow around the building. In the multi-physics BIPV model, $h_{c,f}$ corresponds to the convective heat transfer correlations presented by Montazeri & Blocken (2017). These correlations have been obtained from computational fluid dynamics (CFD) simulations and are valid for isolated buildings. The correlations not only take into account the building geometry, wind speed and wind direction, but also distinguish between windward, leeward and side facades. In contrast to other BIPV models in the literature, three additional factors are thus taken into account in the multi-physics model: the building geometry, the wind direction, and the building surface (with respect to the incoming wind).

Natural convection is the result of the buoyant flow over the BIPV surface and is related to density variations caused by temperature variations. In the multi-physics BIPV model, $h_{c,n}$ is modelled using the following correlation for natural convection for vertical plates (Churchill & Chu, 1975):

$$h_{c,n} = \left(0.825 + 0.325 \mathrm{Ra}_h^{1/6}\right)^2 \tag{13}$$

where Ra_h is the Rayleigh number based on the characteristic length h, which in this case is the height of the BIPV control volume.

Inside the cavity, the variation of the specific enthalpy, h_{air}, of the mass of each air volume, m_{air}, is described as:

$$m_{air} \frac{dh_{air}}{dt} = q_{c,cav1} + q_{c,cav2} + \left(h_{air,ext} - h_{air,in}\right)\dot{m} \tag{14}$$

where $q_{cav,1}$ and $q_{cav,2}$ are the convective heat fluxes between the cavity walls and the air, and $\dot{m}$ is the mass flow rate through the cavity, associated with the enthalpy flux ($h_{air,ext}$ - $h_{air,in}$).

As illustrated in Figure 3, the airflow connects the BIPV control volumes, in a way that $(\dot{m}\ h_{air})_{ext}$ from one control volume is the $(\dot{m}\ h_{air})_{int}$ of the other, except for the first and last control volumes. The temperature of the air entering the BIPV cavity is an input to the multi-physics BIPV model and is discussed later in Section 2.4.

The convective heat fluxes inside the cavity are defined as:

$$q_{c,cav1} = \frac{Q_{c,cav1}}{A} = h_{c,1}\left(T_{s,1} - T_{air}\right) \tag{15}$$

and

$$q_{c,cav2} = \frac{Q_{c,cav2}}{A} = h_{c,2}\left(T_{s,2} - T_{air}\right) \tag{16}$$

where $T_{s,1}$ and $T_{s,2}$ are the surface temperatures of the cavity walls (Figure 5), T_{air} is the temperature of the (well mixed) air volume, and $h_{c,1}$ and $h_{c,2}$ are the convective heat transfer coefficients inside the cavity. Both $h_{c,1}$ and $h_{c,2}$ are modelled using Equation 13.

The radiative heat transfer between the glass surface and building wall surface is defined as:

$$Q_{r,12} = \frac{\sigma\left(T_{s,1}^4 - T_{s,2}^4\right)A}{\frac{1-\varepsilon_1}{\varepsilon_1} + \frac{1}{F_{12}} + \frac{1-\varepsilon_2}{\varepsilon_2}} \tag{17}$$

where $T_{s,1}$ is the glass surface temperature, $T_{s,2}$ is the building wall surface temperature, ε_1 is the glass emissivity, ε_2 is the building wall emissivity, F_{12} is the view factor between the glass and building wall surfaces, and A is the surface area of a BIPV control volume.

Assuming that $F_{12} = 1$, Equation 17 results in:

$$Q_{r,12} = \frac{\sigma\left(T_{s,1}^4 - T_{s,2}^4\right)A}{\frac{1}{\varepsilon_1} + \frac{1}{\varepsilon_2} - 1} \tag{18}$$

Finally, the heat exchange with the building interior is also composed of radiative and convective heat exchanges, as follows:

$$Q_{int} = Q_{c,int} + Q_{r,int} \tag{19}$$

where $Q_{c,int}$ is the convective heat transfer between the BIPV building wall and the building interior and $Q_{r,int}$ is the radiative heat transfer between the BIPV building wall and surfaces composing the building interior. These two heat exchanges are based on the modelling already available in the IDEAS library, as described by Jorissen et al. (2018). Moreover, in this paper, Q_{int} is a measured variable and is used as input to the multi-physics BIPV model, as explained later in Section 2.4.

2.2.2. Airflow modelling

To calculate the airflow rate, the multi-physics BIPV model relates the airflow rate, $\dot{m}$, to the driving pressure differential, ΔP, as follows:

$$\dot{m} = \rho_{air} C \Delta P^n \tag{20}$$

where C is the flow coefficient, which represents the cavity (friction and turbulent) losses, and n is the flow exponent, which represents the flow regime (laminar or turbulent). In this work, a dedicated experimental pressurisation setup has been developed to obtain C and n for the naturally-ventilated BIPV module investigated in this paper (presented later in Section 2.4.2).

In naturally ventilated elements, the driving pressure differential ΔP is a result of buoyancy and wind effects:

$$\Delta P = \Delta P_b + \Delta P_w \tag{21}$$

where ΔP_b is the buoyancy-driven pressure differential and ΔP_w is the wind-driven pressure differential.

Buoyancy is the consequence of density differences between the air inside the cavity and the ambient air. In the multi-physics BIPV model, the resulting buoyancy-induced pressure is computed over all the air volumes in Figure 5, which are considered as well-mixed air volumes, using the following equation:

$$\Delta P_b = g \left[\rho_{ext} H - \sum_{i=1}^{n} \rho_i h_i \right] \tag{22}$$

where g is the gravity force, ρ_{ext} is the exterior air density, H is the total height of the air column inside the cavity, ρ_i is the air density of each BIPV control volume, and h_i is the height of each BIPV control volume (of a total of n control volumes).

The wind-driven pressure is calculated as:

$$\Delta P_w = \Delta C_p V_w^2 \tag{23}$$

where ΔC_p accounts for the wind pressure difference between the openings of the BIPV module and V_w is the wind speed at 10 m height.

The C_p coefficients used in the multi-physics BIPV model are obtained from the CFD simulations performed by Blocken & Carmeliet (2002), as presented by Saelens & Hens (2001). These simulations have been developed specifically for the Vliet test building in which the BIPV module is integrated (as described in Section 2.1). The coefficients correspond to a wind direction perpendicular to the building facade. In this work, this coefficient has been applied to wind coming from any direction within the range of ± 45 deg from the direction perpendicular to the BIPV module. The pressure effects of wind coming from any other direction are not considered. Note that the use of the multi-physics BIPV model for different buildings requires the adaptation of these values.

2.2.3. PV electrical modelling

The one-diode model is adopted in the multi-physics BIPV model as it provides a good balance between complexity and accuracy (Chin et al., 2015). In the one-diode model, the I-V characteristic of a PV device is described by the following implicit transcendental equation:

$$I = I_{ph} - I_{sat}\left[\exp\left(\frac{V + IR_S}{mN_S V_{th}}\right) - 1\right] - \frac{V + IR_S}{R_{sh}} \tag{24}$$

where I and V are the diode current and voltage, I_{ph} is the photo current (or light current), I_{sat} is the (reverse) saturation current, R_S is the series resistance, R_{sh} is the shunt resistance, m is the diode ideality factor, N_S is the number of (identical) cells connected in series, and $V_{th} = \frac{kT}{q}$ is the thermal voltage, with k the Stefan-Boltzmann constant (1.381×10^{-23} J/K), and q the electronic charge (-1.602×10^{-19} C).

The five unknown parameters in Equation 24, i.e. I_{ph}, I_{sat}, m, R_S and R_{sh}, have to be determined. In the multi-physics BIPV model, m, R_S and R_{sh} are assumed constant, independent of temperature and irradiance (Villalva et al., 2009; Orioli & Di Gangi, 2013). To obtain I_{ph}, Equation 24 is considered at short-circuit (SC) conditions. Assuming that I_{sat} and R_S can be neglected at SC (Orioli & Di Gangi, 2013), Equation 24 results in:

$$I_{ph} = I_{SC} \tag{25}$$

with the short-circuit current, I_{SC}, defined as (Villalva et al., 2009):

$$I_{SC} = \frac{G}{G_{STC}}\left[I_{SC,STC} + \mu_{I_{SC}}(T - T_{STC})\right] \tag{26}$$

where G is the solar irradiance, G_{STC} is the irradiance at STC (= 1000 W/m^2), $I_{SC,STC}$ is the short circuit current at STC, $\mu_{I_{sc}}$ is the temperature coefficient of short-circuit current, T is the cell temperature, and T_{STC} is the temperature at STC (= 25 °C).

Once I_{ph} is known, the saturation current, I_{sat}, can be estimated from Equation 24 at open-circuit (OC) conditions. Assuming $R_{sh} \approx \infty$ (Villalva et al., 2009), Equation 24 then becomes:

$$I_{sat} = \frac{I_{SC,STC} + \mu_{I_{SC}}(T - T_{STC})}{\exp\left(\frac{V_{OC,STC}+\mu_{V_{OC}}(T-T_{STC})}{nN_S V_{th}}\right) - 1} \tag{27}$$

with the open-circuit voltage, V_{OC}, defined as (Villalva et al., 2009):

$$V_{OC} = V_{OC,STC} + \mu_{V_{OC}}(T - T_{STC}) \tag{28}$$

where $\mu_{V_{OC}}$ is the temperature coefficient of open-circuit voltage.

To allow the simulation of shading events, the multi-physics BIPV model takes into account spatial variations of solar intensity and temperature within the PV module. For that, the one-diode model is employed at the cell level by adjusting the parameters used in Equations 24-27 to correspond to a single PV cell. The electrical parameters are summarised in Table 1. I_{SC} and V_{OC} have been determined experimentally, while typical values for c-Si cells are used for m, R_S and R_{sh}. The BIPV power at STC, P_{STC}, is also listed in Table 1.

Finally, the multi-physics BIPV model employs a perturb-and-observe (P&O) algorithm to track the maximum power point by varying the load connected to the module. The algorithm is available in the Open Source PhotoVoltaics Library for Systemic Investigations, an open-source Modelica library (Brkic et al., 2019). The maximum power point tracker (MPPT) algorithm adjusts the PV electric operating point for every simulation step. Every time the MPPT algorithm acts, a time event is triggered and the entire system of equations is solved (including thermal and airflow coupling). The simulation time step is discussed later in Section 2.4.

Table 1: Electrical parameters. *I_{SC}, V_{OC} and P_{STC} have been determined experimentally with an accuracy of 10 % due to irradiance uniformity and current sweep.

Parameter	Value	
I_{SC} (cell)	8.25*	A
V_{OC} (cell)	0.62*	V
R_S (cell)	0.0067	Ω
R_{sh} (cell)	∞	Ω
m (cell)	1.1	-
P_{STC} (BIPV module)	70.6*	W

2.3. Experimental setup

Figure 6 shows a schematic representation of the experimental setup and Table 2 summarises the characteristics and accuracy of the measurement equipment. The measured dataset correspond to three summer months in 2017. The next subsections describe the experimental data in detail, including weather conditions, power, temperature and heat flux measurements.

2.3.1. Weather conditions

The weather conditions include the ambient temperature, the wind speed and direction, and the solar irradiance on the BIPV facade. As illustrated in Figure 6, ambient temperature is recorded with a resolution of 60 s by the weather station located on the roof of the building (about 5 m above the flat part of the roof). The wind speed and direction are monitored by a ultrasonic anemometer located at 10 m height, in the open field in front of the BIPV facade. Wind conditions are recoded with a resolution of 300 s. A pyranometer located next to the BIPV module measures the solar irradiance on the facade every 10 s. Table 3 reports the average weather conditions over the measuring period for each month. These data form the weather input data used in the multi-physics BIPV model. As mentioned previously, the simulations employ a time step

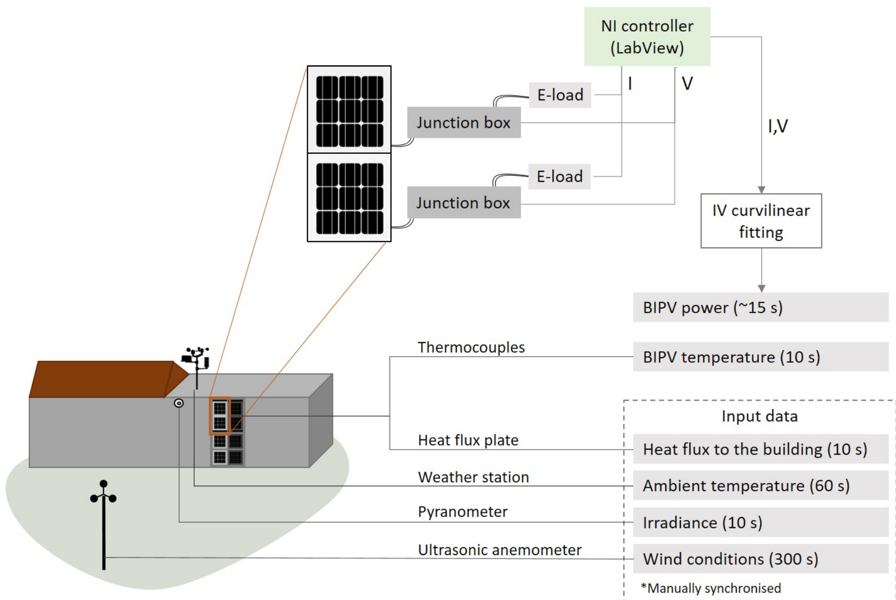

Figure 6: Overview of the experimental setup (not to scale).

Table 2: Characteristics and accuracy of the measurement equipment.

Variable	Equipment/Sensor	Time resolution	Accuracy	
Ambient temperature	Hygroclip 2L	60 s	± 0.2 K	
Wind speed	Ultrasonic anemometer Gill Windmaster	300 s	0-20 m/s	1.5 %
			20-35 m/s	1.5-3 %
			35-60 m/s	3 %
Wind direction	Ultrasonic anemometer Gill Windmaster	300 s	<25 m/s	± 2 deg
			>25 m/s	± 4 deg
Solar irradiance	Thermopile pyranometer type CMP Kipp & Zonen	10 s	<3 %	
Surface and air temperatures	Thermocouple Type T Class 1	10 s	± 0.5 K	
Heat flux	Hukseflux heat flux plate	10 s	± 3 %	
Power	Electronic loads + NI controller	∼15 s	∼0.6 % (MPP) ∼4 % low-irradiance	

of 10 s, which corresponds to the resolution of the irradiance data; the other variables are interpolated using Akima splines (continuous first derivative).

Table 3: Average daily weather conditions for each month of the experimental data.

	Solar irradiance [W/m^2]	Ambient temperature [°C]	Wind speed [m/s]
June	139.0	20.2	1.9
July	116.0	19.8	1.6
August	107.8	19.2	0.9

2.3.2. Power measurements

As illustrated in Figure 6, the acquisition of I-V data is made via LabView using electronic loads (E-loads) with variable resistances and a controller from National Instruments (NI). The E-loads operate in constant current mode and are controlled using a NI real-time controller running a LabView-based software. First, the short-circuit current of each module is measured. Then, the I-V curves are swept backwards, starting at 10 % above the short circuit current and ending at open circuit. The module voltages at the junction boxes are measured by the NI controller in differential mode, using 4-wire probing. The I-V curve sweeping takes about 5-6 s, which leads to a non-uniform interval of about 15 s for the power data. The maximum power is determined by curvilinear fitting of I-V curves (containing 50 points each). For further information on this procedure, the reader is addressed to Spiliotis et al. (2017).

2.3.3. Temperature and heat flux measurements

The scheme in Figure 7 indicates the location of the thermocouples and the heat flux meter. The BIPV surface temperature is measured at five different positions at the back of each mini-module, as shown in the figure. The insulation surface temperature on the cavity side is measured at the middle section at three locations, also equidistant over the height (bottom, middle and top). The air temperature is monitored at both openings as well as inside the cavity at the middle section at three equidistant points over the BIPV height (bottom, middle and top). Surface and air temperatures are measured using Type T class 1 thermocouples and the heat flux to the building interior is measured by a heat flux plate, both with a time resolution of 10 s. Note that surface measurements at the back of the mini-modules refer to the glass surface and not to the PV cell temperature.

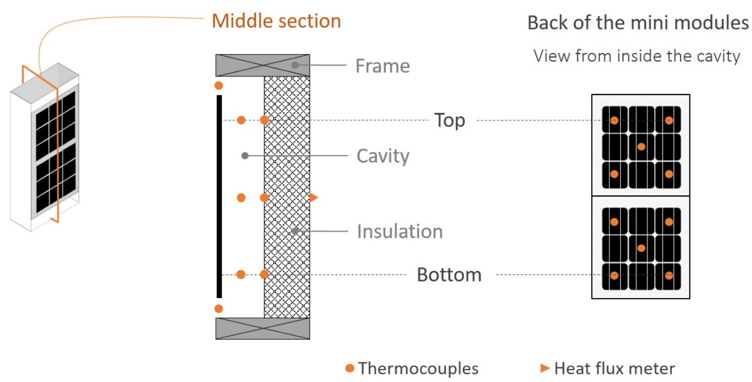

Figure 7: The BIPV module and the experimental instrumentation, including thermocouples and heat flux meter. For the sake of clarity, the thermocouples at the back of the PV modules are omitted in the middle section and are only shown in the view from inside the cavity.

The quality of contact measurements can be evaluated by assessing the so-called installation errors, which are associated with the following aspects (Bentley, 1995; Saelens, 2002; AlWaaly et al., 2015): (1) the thermal contact resistance between the glass and the thermocouple, (2) the relative position of the thermocouple compared to the thermal gradient, and (3) the fin effect of the thermocouple wire. Because thermo-optical properties of the tape differ from the module properties, solar irradiation may also cause measurement errors, as discussed by Saelens (2002) and Kalyanova (2008). In order to reduce the installation errors, the thermocouples were tightly attached to the glass surface using tape, as recommended by Herteleer (2016), and the wires of the thermocouples were placed parallel to the respective isotherm (at each vertical position), as suggested by Saelens (2002). Because the white encapsulant used in the BIPV module is not completely opaque to the solar radiation, the thermocouples inside the cavity are vulnerable to the transmitted radiation. In order to reduce this effect, reflective tape was used to attach the thermocouples to the surfaces, and cylindrical aluminum shells were used to shield the thermocouples measuring the air temperature.

2.4. Inputs to the multi-physics BIPV model

2.4.1. Material properties

Table 4 lists the material properties of the BIPV module used in the multi-physics BIPV model. Note that the building wall in the BIPV module corresponds to a single insulation layer.

Table 4: Material properties of the BIPV module.

	Glass	PV cell	Insulation
Thickness [m]	0.003	0.0001	0.15
Thermal conductivity [W/mK]	0.96	710	0.036
Heat capacity [J/kgK]	750	710	840
Density [kg/m^3]	2500	2330	110
Short-wave emissivity [-]	0.95	-	-
Long-wave emissivity [-]	0.9	-	0.8
Reflectivity [-]	0.8	-	-

2.4.2. Experimental pressure characterisation

As explained in Section 2.2.2, the airflow model requires two parameters, namely the flow coefficient C and the flow exponent n. To obtain these parameters for the BIPV module investigated in this paper, an experimental pressurisation setup was developed, as illustrated in Figure 8a. Table 5 summarises the characteristics and accuracy of the equipment used for the pressurisation tests.

Figure 8a shows that, at the bottom of the BIPV module, a fan imposes a (known) airflow rate through the cavity. At the top, the cavity is open to the atmospheric pressure. A pair of pressure taps records the pressure difference

Table 5: Characteristics and accuracy of the measuring equipment

Variable	Equipment	Time resolution	Accuracy
Pressure difference	Pressure gauges (Halstrup Walcher)	10 s	± 0.3 Pa
Airflow rate	Hot film anemometer (Lindab LT600)	1 s	0.0009 l/s or 5 %, whichever is greater

over the cavity associated with the imposed airflow. The relationship between the two measured variables - airflow rate and pressure difference - determines the so-called cavity pressure characteristic (i.e. C and n). The plenum box in Figure 8a helps to create a region of uniform pressure at the bottom opening, attenuating the directionality effect of the fan.

Figure 8b presents the results from six pressurisation tests together with the power law to which they fit. A theoretical restriction is imposed on the flow exponent n, which should be within the interval [0.5, 1], from laminar to turbulent flow. The coefficients C and n indicated in Figure 8b are used in the multi-physics BIPV model to obtain the airflow as a function of the driving pressure (Equation 20).

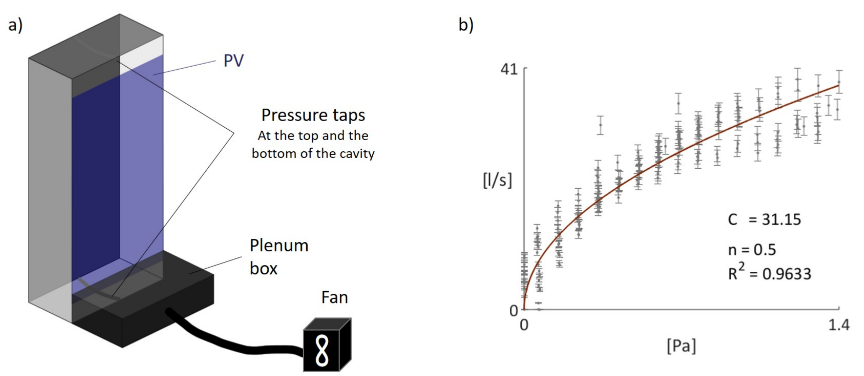

Figure 8: a) Schematic representation of the experimental pressurisation setup. b) Resulting airflow rate as a function of the pressure difference over the cavity height.

2.4.3. Additional assumptions

As mentioned previously, the heat transfer to the building is not included in the simulations (*building interior* side in Figure 5). Instead, the heat flux measured at the middle of the building wall (shown in Figure 7) is imposed on the wall layer of all BIPV control volumes. Additionally, experimental results presented by Saelens et al. (2004) have shown that the inlet air temperature is different from the ambient temperature for ventilated facades due to local heating. Such local effects may also be critical in this work, since the BIPV module used for the validation is part of a facade setup comprising several modules, as shown in Figure 2. The buoyancy effects from the adjacent BIPV modules may affect the temperature at the cavity inlet. Hence, the air temperature measured at the bottom of the cavity (Figure 7) is used as inlet temperature in the model.

2.4.4. Simulation time step

Running the simulations at small time steps may be necessary to capture the influence of highly varying conditions, if present in the weather input dataset. In the multi-physics BIPV model, the time steps was set to 10 s to match the time resolution of the irradiance input, which is the highest resolution of the input dataset (see Table 2). This means that the boundary conditions on the BIPV module change every 10 s. Since thermal dynamics also affect the BIPV module state in the model, the use of a time steps of 5 s has been tested, but did not influence the results. Note that for the weather variables in the input data that have different time resolutions (i.e. ambient temperature and wind conditions), the data is interpolated using Akima splines such that the first derivative is continuous.

3. Results

3.1. Power and energy yield

First, the power profiles over time are presented in order to provide visual insight into the results. For that, six consecutive days in June are selected:

two clear-sky days and four cloudy days. The solar irradiance on the BIPV facade and the ambient temperature measured during these six days are shown in Figure 9.

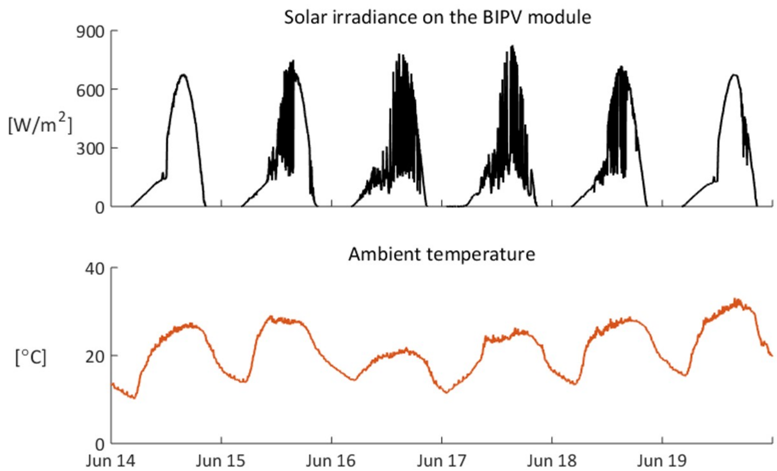

Figure 9: Solar irradiance on the BIPV facade and ambient temperature for the six days in June 2017.

The power profiles are presented in Figure 10. This figure compares predictions of the multi-physics BIPV model to the measurements. The linear power model described in Appendix A is also included in the comparison as a reference. For the two clear sky days (Jun 14 and Jun 19), the multi-physics BIPV model provides relatively good predictions, while the power model underestimates the measured power. For cloudy days, visualising the results is not straightforward, but the errors are quantified later on.

Figure 10b shows two interesting aspects. First, these plots illustrate the effects of vertical integration in a southwest facade: the peak in solar irradiance occurs late in the afternoon. During most of the morning period, the facade only receives diffuse irradiance. When the direct irradiance starts to reach the facade around late morning, a steep raise in the BIPV power is observed. Second, also when the sun starts to directly reach the facade, the pyranometer is shaded by an equipment bar that is attached perpendicularly to the building. The reduction in irradiance is propagated into the model predictions (both multi-physics and power models), while the measurements do not show any reduction, since the BIPV module itself is not shaded.

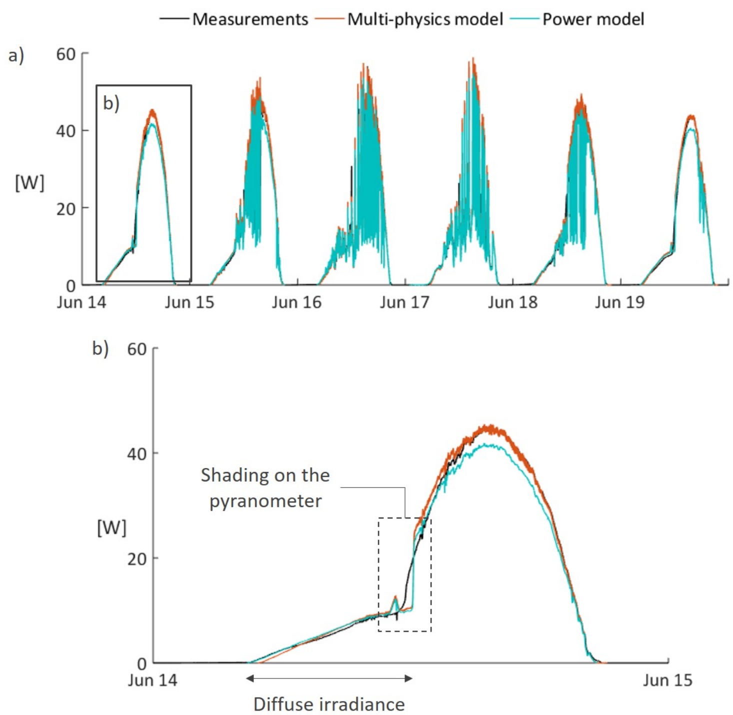

Figure 10: a) BIPV power for six days in June: Comparison between measurements and predictions from the multi-physics BIPV model and the power model. b) Zoom into one day for better visualisation of the results.

Also note that the power model has the (surface-average) back-of-module temperature measurements as input. In the absence of temperature measurements, the BIPV temperature has to be estimated either using a physics-based approach or an (semi-)empirical temperature correlation (as the ones reviewed by Skoplaki & Palyvos (2009)). In contrast, the multi-physics BIPV model couples the cell temperature to the power estimations, solving the two variables simultaneously, as described in Section 2.2.

Next, the energy yield is calculated at both daily and monthly basis by numerically integrating the power results over time. The difference in energy yield between measurements and model predictions corresponds to the total error (TE). TE can be negative or positive, indicating under or overestimations. The mean relative error (MRE) is the ratio between the absolute yield difference (i.e. absolute total error) and the measured yield (thus, always positive).

The relative errors in monthly energy yield estimations are presented in Table 6. To calculate this indicator, the power predictions and the measurements are integrated over each month and compared to each other. For the multi-physics BIPV model, the relative error in the estimations of monthly energy yields remains well below 2 %. For the power model with P_{STC} = 70.6 W_P (Table 1), the monthly error exceeds 5 % in all months. Due to the uncertainty in the determination of the nominal power (see Table 1), results for 1.05 P_{STC} are included in Table 6, showing how sensitive the power model is to the correct determination of this parameter.

Table 6: Monthly energy yield: Relative error [%].

	Jun	Jul	Aug
Multi-physics BIPV model	0.74	0.41	1.20
Power model (P_{STC})	-5.15	-5.75	-5.15
Power model (1.05 P_{STC})	-0.41	-1.04	-0.41

For the multi-physics BIPV model, Figure 11 presents TE and MRE results for the daily energy yield estimations (again, numerically integrated over each day in the dataset). The average daily error is 1.79 % in June, 2.55 % in July, and 2.56 % in August. While the TE is generally of the same order of magnitude (± 10 Wh), some days present MRE values significantly above the average (in particular July 1, August 8, and August 10). These days are characterised by a low daily solar irradiation, below 500 Wh/m^2. For similar TE values, such low irradiation leads to higher MRE due to the relative nature of this indicator. Nevertheless, apart from these three days, MRE remains mostly below 5 %.

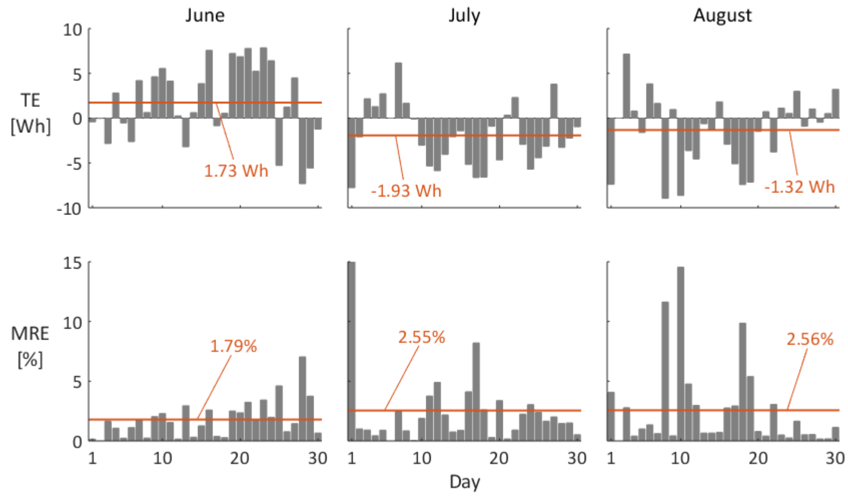

Figure 11: Daily energy yield for the whole dataset: Total error (TE) and mean relative error (MRE) between the measurements and the multi-physics BIPV model (July 6 and August 2 have been omitted due to lack of measured data).

3.2. Temperature results

Again, for the visual evaluation of the results, Figure 12 presents the back-of-module temperature profiles for the same days in June (Figure 9). Back-of-module temperature refers to $T_{s,1}$ in Figure 5. Here, the (semi-)empirical temperature models described in Appendix B are included in the comparative analysis as reference. For the sake of clarity, the predictions of the multi-physics BIPV model are first compared only to the measurements (Figure 12a). Next, in Figure 12b, the Ross' (Eq. B.1) and Skoplaki et al.'s (Eq. B.2) models are added to the comparison. Last, Figure 12c zooms into two days to provide a more clear visualisation.

Overall, a good agreement is observed between the multi-physics BIPV model predictions and the measurements for the back-of-module temperature. The two (semi-)empirical models overestimate the measurements. In addition, Figure 12 demonstrates that the multi-physics model is also able to predict the temperature dynamics, while the Ross' model is only able to do so for clear sky days, such as June 14 presented in Figure 12c. Compared to the Ross' model, the Skoplaki et al.'s model presents fluctuations in temperature due to the incorporation of wind speed.

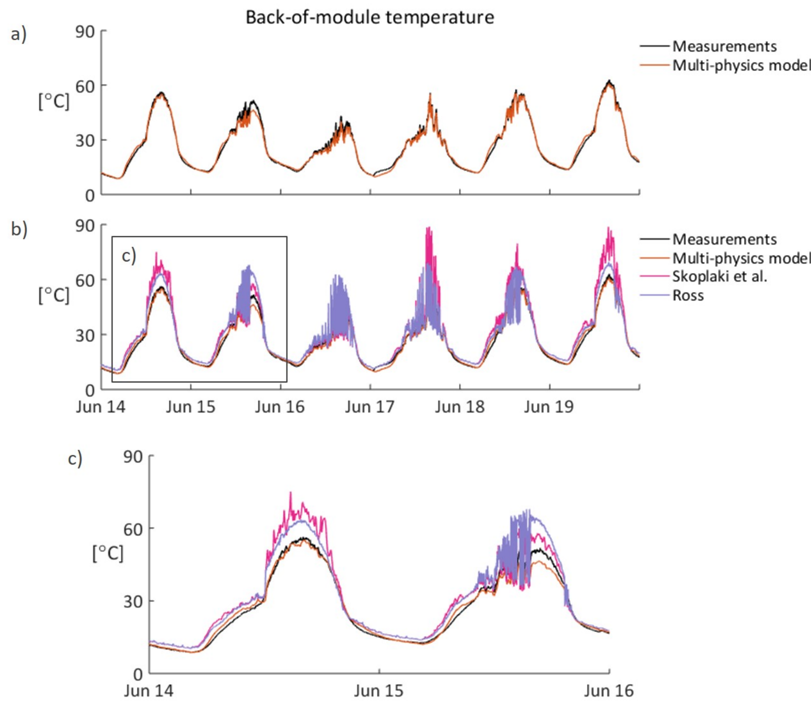

Figure 12: Back-of-module temperature for six days in June: a) Comparison between measurements and the multi-physics BIPV model. b) Same as a) including the predictions from the Ross' model (Ross, 1976; Nordmann & Clavadetscher, 2003) and Skoplaki et al.'s model (Skoplaki et al., 2008). c) Zoom into two days for better visualisation.

Figure 13 presents the difference in back-of-module temperature between the measurements and each one of the three models for the whole month of June. The average and maximum differences are also indicated (average values are presented later in Table 7 for the three months). Among the three models, the multi-physics model (Figure 13a) provides the better agreement, with lowest average and maximum differences (-0.60 and 12.4 °C, respectively). Both Ross' (Figure 13b) and Skoplaki et al.'s (Figure 13c) models generally overestimate the module temperature (averages of 2.81 and 3.12 °C, respectively), with maximum differences up to 40 and 50 °C, respectively. The models by Ross' and

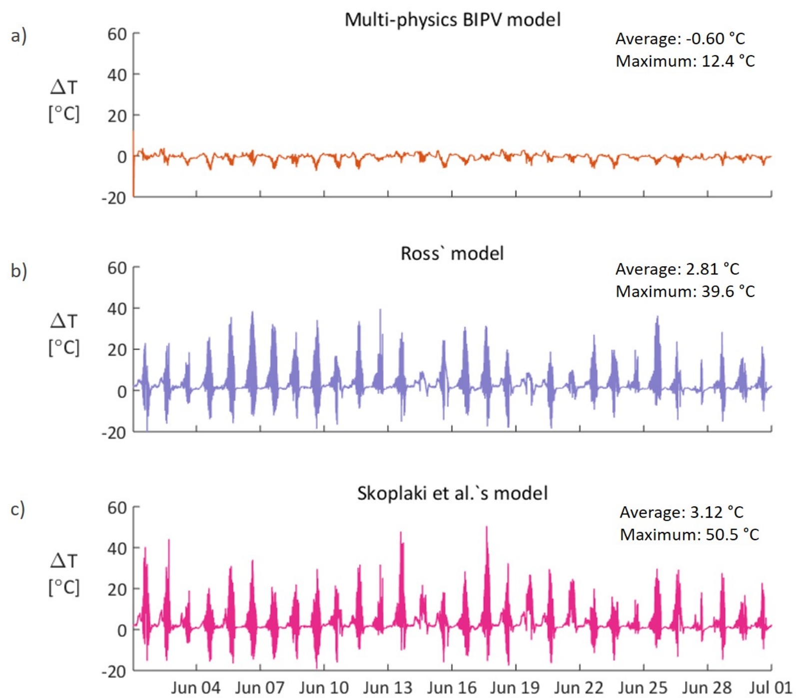

Figure 13: Difference in back-of-module temperature compared to the measurements for six days in June: a) multi-physics model, b) Ross' model, and c) Skoplaki et al.'s model.

Skoplaki et al. are based on data from a BIPV facade with limited ventilation presented b Nordmann & Clavadetscher (2003), which might explain the higher temperatures obtained from these two models.

Next, temperature results are analysed for the whole dataset in terms of absolute differences. Relative differences are not suitable for temperature analysis, as they depend on the temperature scale (Kelvin scale resulting in lower relative differences compared to Celsius scale). Table 7 presents the results for the back-of-module temperature for the three models, for the three months in the measured dataset. The multi-physics BIPV model estimates the back-of-module temperature with a MAE within 1.0-2.5 °C and a RMSE within 1.5-4.5 °C. The Ross' model presents a MAE between 3.0-3.5 °C and a RMSE between 5.0 and 5.5 °C. The Skoplaki et al.'s model presents a MAE between 3.5-4.5 °C and a RMSE between 5.5 and 7.5 °C. Compared to the mean absolute error (MAE),

Table 7: Back-of-module temperature results: Average difference, MAE, and RMSE (all in °C). The differences are plotted in Figure 13 for June.

	Average difference			MAE			RMSE		
Model	Jun	Jul	Aug	Jun	Jul	Aug	Jun	Jul	Aug
Multi-physics	-0.60	-1.32	-1.62	1.11	2.40	2.18	1.91	4.23	3.77
Ross	2.81	2.91	2.31	3.37	3.48	3.09	5.21	5.47	5.04
Skoplaki et al.	3.12	3.31	3.77	3.66	3.82	4.32	5.66	6.10	7.41

Table 8: Air and wall temperatures: Comparison between the multi-physics BIPV model and measurements.

	Average difference			MAE			RMSE		
Surface	Jun	Jul	Aug	Jun	Jul	Aug	Jun	Jul	Aug
Wall ($T_{s,2}$)	-0.08	-0.82	-1.39	0.74	1.96	1.89	1.04	3.71	3.32
Air (T_{air})	-1.58	-0.75	-1.08	2.07	1.88	1.66	3.43	3.61	2.92

the square formulation of the root mean squared error (RMSE) emphasises larger differences.

For the multi-physics BIPV model, the cavity air temperature (T_{air} in Figure 5) and the surface temperature of the building wall ($T_{s,2}$ in Figure 5) are also evaluated. As presented in Table 8, a generally good agreement between measurements and predictions is obtained for T_{air} and $T_{s,2}$. The (semi-)empirical models do not provide such information and are, thus, not included in this analysis.

4. Discussion

For the naturally ventilated BIPV module investigated in this work, the multi-physics BIPV model is able to predict the BIPV energy yield and back-of-module temperature within an acceptable error range for building performance simulations. In addition, the multi-physics BIPV model provides a good agreement for the cavity air and wall temperatures. The air temperature is an important variable if the cavity air is used as heat source for space heating, while the wall temperature is an important boundary condition on the building thermal performance. An ongoing effort in this context is the simulation of BIPV envelopes combining the multi-physics BIPV model with the building models available in the IDEAS library.

The results in this paper are associated with a specific BIPV module and a specific experimental data. Using additional experimental data is certainly important to further verify the reliability of the multi-physics BIPV model. Note that, the three summer months presented here are already a relevant period for BIPV operation in view of their annual energy share. Furthermore, physics-based models are generally less data intensive. Future work will nevertheless consider different BIPV modules operating under different conditions. This effort is supported by the flexible and modular environment provided by IDEAS/Modelica library. Such flexibility enables the adaptation of the multi-physics BIPV model to a mechanically ventilated or unventilated variant, for example. Furthermore, differently from the conventional approach in building performance simulation, the PV elementary unit developed in this work has the dimensions of a PV cell. In this way, BIPV modules of different sizes can also be simulated.

To enable the simulation of shading events, the multi-physics BIPV model takes into account the spatial variation of solar intensity and temperature at the cell level. However, it is important to stress that, while the model is able to simulate shading effects, the experimental BIPV setup investigated in this paper is mostly free of shading. Therefore, shading effects are not present in the experimental data. Previous research has shown that a high-resolution electrical model such as the one employed in the multi-physics BIPV model is capable of simulating PV systems under complex shading conditions (Sprenger et al., 2016; Gallardo-Saavedra & Karlsson, 2018; Walker et al., 2019). Detailed investigations on the impact of shading effects are beyond the scope of this paper, but are part of ongoing research efforts.

This paper also investigates simplified models available in the literature for the estimation of the BIPV power and (back-of-module) temperature. In terms of energy yield predictions, the linear power model predicts the BIPV energy yield with slightly larger errors. However, the power model depends on accurate STC data and accurate temperature estimations. In terms of back-of-module temperature predictions, (semi-)empirical temperature correlations generally overestimate the measurements. Moreover, empirical correlations do not provide information on the air and wall temperatures. The advantage of simplified models is that they do not require detailed data and do not demand significant computational resources. In contrast, the multi-physics BIPV model requires detailed information about the BIPV module and its environment, such as geometry, construction aspects, wind pressure coefficients, etc. The high-resolution detailed modelling also poses challenges concerning the total simulation time.

The observations above have to be put into perspective to the goal of the analysis (research vs. engineering goal), the design stage of the project (early vs. late stage), and the scale of the problem (module vs. building vs. district level). Conducting representative simulations at building/district level involves a more complex system, where minor variations in the BIPV daily energy yield may not be relevant for the whole system performance and the total simulation time may be a more important constrain. In such cases, simplified models may be more appropriate, possibly in combination with a simplified method that accounts for shading losses, e.g. Zomer & Rüther (2017a), Zomer & Rüther (2017b). In contrast, assessing the integration of the BIPV power into the electrical grid may require a higher degree of accuracy and time and space resolution. For these applications, broadening the scope of the electrical model may be more relevant, e.g. Sprenger et al. (2016), Walker et al. (2019).

5. Conclusion

The main contribution of this work is the development of a multi-physics BIPV model for facade applications within a building performance simulation environment. The model combines a high-resolution electrical model with physics-based thermal and airflow models. This work was motivated by a general trend observed in BIPV models that focus either on a high-resolution electrical model or on a detailed thermal model. The combination of both approaches is not common in BIPV modelling, particularly in the context of building performance simulations.

In summary, the characteristics of the multi-physics BIPV model are the following: (1) thermal coupling between the BIPV module and the building indoor environment; (2) high resolution electrical model (temperature-dependent one-diode at cell level); (3) the possibility of simulating shading effects intra and inter-modules; (4) the modelling of external heat transfer considering both buoyancy and wind effects, the latter taking into account the building geometry, wind speed and direction, and the building surface with respect to incoming wind flow; (5) a detailed modelling of the airflow through the cavity based on experimental pressurisation data, including both buoyancy and wind effects.

The multi-physics BIPV model predictions are compared to three months of experimental data from a realistic BIPV facade implementation. A good agreement is observed for daily energy yield as well as for temperature predictions. On average, the BIPV daily energy yield is estimated with an error below 3 % and the monthly energy yield with an error below 2 %. The back-of-module PV temperature is predicted with a MAE lower than 2 °C and RMSE lower than 5 °C. Similar results are verified for the air temperature inside the cavity and the building wall temperature (inside the cavity).

6. Acknowledgments

This work has been conducted within the EFRO SALK project, supported by the EU, ERDF, Flanders Innovation & Entrepreneurship and the Province of Limburg. Within this project, the authors acknowledge the collaboration with the Department of Electrical Engineering (ESAT) from KU Leuven as well as with the research group PV modules and systems from imec. Regarding the experimental work, the authors also recognise the important role of our technicians Wim Bertels, Patricia Elsen and Jimmy Van Criekingen. Twan van

Hooff is currently a postdoctoral fellow of the Research Foundation Flanders (FWO) and acknowledges its financial support (project FWO 12R9718N).

Appendix A. Linear power model

The power model is calculated as follows:

$$P = \eta_{ref}[1 - \beta(T - T_{ref})]AG, \tag{A.1}$$

with

$$\eta_{ref} = \frac{P_{STC}}{G_{ref}A}, \tag{A.2}$$

where η_{ref} is the module efficiency at STC, T is the temperature of the module, T_{ref} is the reference temperature (= 25 °C), β is the temperature coefficient of power (= 0.42 %/K), A is the PV module area, G is the actual solar irradiance on the BIPV modules (plane-of-array irradiance), and G_{ref} is the reference irradiance (= 1000 W/m^2).

In this model, T is an input, which in this paper corresponds to the (surface-average) back-of-module temperature measurements. No correction is applied to obtain the cell temperature from back-of-module measurements.

Appendix B. Empirical temperature correlations

The following two (semi-)empirical models are used to obtain the BIPV temperature:

(1) Ross' model, which defines the module temperature as (Ross, 1976):

$$T_{BIPV} = T_{amb} + kG, \tag{B.1}$$

where T_{amb} is the ambient temperature, G is the plane-of-array irradiance, and k = 0.0538 (Nordmann & Clavadetscher, 2003; Skoplaki & Palyvos, 2009).

(2) Skoplaki et al.'s model, which includes the wind speed (WS) in the equation, as follows (Skoplaki et al., 2008):

$$T_{BIPV} = T_{amb} + \omega G \frac{0.32}{8.91 + 2WS}, \tag{B.2}$$

where T_{amb} is the ambient temperature, G is the plane-of-array irradiance, and $\omega = 2.4$.

References

Agathokleous, R. A., & Kalogirou, S. A. (2016). Double skin facades (DSF) and building integrated photovoltaics (BIPV): A review of configurations and heat transfer characteristics. *Renewable Energy*, *89*, 743–756.

Agathokleous, R. A., & Kalogirou, S. A. (2018a). Part i: Thermal analysis of naturally ventilated bipv system: Experimental investigation and convective heat transfer coefficients estimation. *Solar Energy*, *169*, 673–681.

Agathokleous, R. A., & Kalogirou, S. A. (2018b). Part ii: Thermal analysis of naturally ventilated bipv system: Modeling and simulation. *Solar Energy*, *169*, 682–691.

Aguacil, S., Lufkin, S., & Rey, E. (2019). Active surfaces selection method for building-integrated photovoltaics (bipv) in renovation projects based on self-consumption and self-sufficiency. *Energy and Buildings*, *193*, 15–28.

Alrashidi, H., Ghosh, A., Issa, W., Sellami, N., Mallick, T. K., & Sundaram, S. (2020). Thermal performance of semitransparent cdte bipv window at temperate climate. *Solar Energy*, *195*, 536–543.

AlWaaly, A. A., Paul, M. C., & Dobson, P. S. (2015). Effects of thermocouple electrical insulation on the measurement of surface temperature. *Applied Thermal Engineering*, *89*, 421–431.

Assoa, Y.-B., & Ménézo, C. (2014). Dynamic study of a new concept of photovoltaic–thermal hybrid collector. *Solar energy*, *107*, 637–652.

Assoa, Y. B., Sauzedde, F., & Boillot, B. (2018). Numerical parametric study of the thermal and electrical performance of a bipv/t hybrid collector for drying applications. *Renewable energy*, *129*, 121–131.

Athienitis, A. K., Barone, G., Buonomano, A., & Palombo, A. (2018). Assessing active and passive effects of façade building integrated photovoltaics/thermal systems: Dynamic modelling and simulation. *Applied Energy*, *209*, 355–382.

Bentley, J. P. (1995). *Principles of measurement systems*. Harlow: Addison Wesley Longman Ltd.

Bergman, T. L., Incropera, F. P., DeWitt, D. P., & Lavine, A. S. (2011). *Fundamentals of heat and mass transfer*. John Wiley & Sons.

Biyik, E., Araz, M., Hepbasli, A., Shahrestani, M., Yao, R., Shao, L., Essah, E., Oliveira, A. C., del Caño, T., Rico, E. et al. (2017). A key review of building integrated photovoltaic (BIPV) systems. *Engineering science and technology, an international journal*, *20*, 833–858.

Blocken, B., & Carmeliet, J. (2002). Spatial and temporal distribution of driving rain on a low-rise building. *Wind and Structures*, *5*, 441–462.

Brito, M., Freitas, S., Guimarães, S., Catita, C., & Redweik, P. (2017). The importance of facades for the solar PV potential of a Mediterranean city using LiDAR data. *Renewable Energy*, *111*, 85–94.

Brkic, J., Ceran, M., Elmoghazy, M., Kavlak, R., Haumer, A., & Kral, C. (2019). Open source photovoltaics library for systemic investigations. In *Proceedings of the 13th International Modelica Conference, Regensburg, Germany, March 4–6, 2019* 157. Linköping University Electronic Press.

Buonomano, A., De Luca, G., Montanaro, U., & Palombo, A. (2016). Innovative technologies for nzebs: An energy and economic analysis tool and a case study of a non-residential building for the mediterranean climate. *Energy and Buildings*, *121*, 318–343.

Chin, V. J., Salam, Z., & Ishaque, K. (2015). Cell modelling and model parameters estimation techniques for photovoltaic simulator application: A review. *Applied Energy*, *154*, 500–519.

Churchill, S. W., & Chu, H. H. (1975). Correlating equations for laminar and turbulent free convection from a vertical plate. *International journal of heat and mass transfer*, *18*, 1323–1329.

d'Alessandro, V., Di Napoli, F., Guerriero, P., & Daliento, S. (2015). An automated high-granularity tool for a fast evaluation of the yield of pv plants accounting for shading effects. *Renewable Energy*, *83*, 294–304.

Defaix, P., Van Sark, W., Worrell, E., & de Visser, E. (2012). Technical potential for photovoltaics on buildings in the eu-27. *Solar Energy*, *86*, 2644–2653.

Defraeye, T., Blocken, B., & Carmeliet, J. (2011). Convective heat transfer coefficients for exterior building surfaces: Existing correlations and CFD modelling. *Energy Conversion and Management*, *52*, 512–522.

Delisle, V., & Kummert, M. (2016). Cost-benefit analysis of integrating bipv-t air systems into energy-efficient homes. *Solar Energy*, *136*, 385–400.

Didoné, E. L., & Wagner, A. (2013). Semi-transparent PV windows: A study for office buildings in Singapore. *Energy and Buildings*, *67*, 136–142.

Díez-Mediavilla, M., Rodríguez-Amigo, M., Dieste-Velasco, M., García-Calderón, T., & Alonso-Tristán, C. (2019). The PV potential of vertical façades: A classic approach using experimental data from Burgos, Spain. *Solar Energy*, *177*, 192–199.

Emmel, M. G., Abadie, M. O., & Mendes, N. (2007). New external convective heat transfer coefficient correlations for isolated low-rise buildings. *Energy and Buildings*, *39*, 335–342.

openIDEAS environment (). OpenIDEAS: An open framework for integrated building and district energy simulations. URL: `https://github.com/open-ideas`.

EPBD (2010). Directive 2010/31/EU of the European Parliament and of the Council of 19 May 2010 on the energy performance of buildings (recast). *Official Journal of the European Union*, *18*, 2010.

Gallardo-Saavedra, S., & Karlsson, B. (2018). Simulation, validation and analysis of shading effects on a pv system. *Solar Energy*, *170*, 828–839.

Ghosh, A., Sarmah, N., Sundaram, S., & Mallick, T. K. (2019). Numerical studies of thermal comfort for semi-transparent building integrated photovoltaic (bipv)-vacuum glazing system. *Solar Energy*, *190*, 608–616.

Goverde, H., Goossens, D., Govaerts, J., Catthoor, F., Baert, K., Poortmans, J., & Driesen, J. (2017). Spatial and temporal analysis of wind effects on PV modules: Consequences for electrical power evaluation. *Solar Energy*, *147*, 292–299.

Herteleer, B. (2016). *Outdoor thermal and electrical characterisation of photovoltaic modules and systems*. Ph.D. thesis KU Leuven.

Hofer, J., Groenewolt, A., Jayathissa, P., Nagy, Z., & Schlueter, A. (2016). Parametric analysis and systems design of dynamic photovoltaic shading modules. *Energy Science & Engineering*, *4*, 134–152.

Horváth, I. T., Goverde, H., Manganiello, P., Govaerts, J., Tous, L., Aldalali, B., Vörösházi, E., Szlufcik, J., Catthoor, F., & Poortmans, J. (2018). Photovoltaic energy yield modelling under desert and moderate climates: What-if exploration of different cell technologies. *Solar Energy*, *173*, 728–739.

Hu, Z., He, W., Ji, J., Hu, D., Lv, S., Chen, H., & Shen, Z. (2017). Comparative study on the annual performance of three types of building integrated photovoltaic (BIPV) trombe wall system. *Applied energy*, *194*, 81–93.

Ioannidis, Z., Buonomano, A., Athienitis, A., & Stathopoulos, T. (2017). Modeling of double skin façades integrating photovoltaic panels and automated roller shades: Analysis of the thermal and electrical performance. *Energy and Buildings*, *154*, 618–632.

Iousef, S., Montazeri, H., Blocken, B., & van Wesemael, P. (2019). Impact of exterior convective heat transfer coefficient models on the energy demand prediction of buildings with different geometry. In *Building Simulation* (pp. 797–816). Springer volume 12.

Jelle, B. P., Breivik, C., & Røkenes, H. D. (2012). Building integrated photovoltaic products: A state-of-the-art review and future research opportunities. *Solar Energy Materials and Solar Cells*, *100*, 69–96.

Jorissen, F., Reynders, G., Baetens, R., Picard, D., Saelens, D., & Helsen, L. (2018). Implementation and verification of the IDEAS building energy simulation library. *Journal of Building Performance Simulation*, (pp. 1–20).

Kalyanova, O. (2008). *Double-skin facade: Modelling and experimental investigations of thermal performance*. Ph.D. thesis Department of Civil Engineering, Aalborg University.

Ma, M., Cai, W., & Wu, Y. (2018). China Act on the energy efficiency of civil buildings (2008): A decade review. *Science of The Total Environment*, *651*, 42–60.

Masson, G., & Brunisholz, M. (2015). Snapshot of global photovoltaic markets. *Report IEA PVPS T1–T292016*, *1*.

Mirsadeghi, M., Costola, D., Blocken, B., & Hensen, J. L. (2013). Review of external convective heat transfer coefficient models in building energy simulation programs: implementation and uncertainty. *Applied Thermal Engineering*, *56*, 134–151.

Miyazaki, T., Akisawa, A., & Kashiwagi, T. (2005). Energy savings of office buildings by the use of semi-transparent solar cells for windows. *Renewable energy*, *30*, 281–304.

Montazeri, H., & Blocken, B. (2017). New generalized expressions for forced convective heat transfer coefficients at building facades and roofs. *Building and Environment*, *119*, 153–168.

Montazeri, H., & Blocken, B. (2018). Extension of generalized forced convective heat transfer coefficient expressions for isolated buildings taking into account oblique wind directions. *Building and Environment*, *140*, 194–208.

Montazeri, H., Blocken, B., Derome, D., Carmeliet, J., & Hensen, J. L. (2015). CFD analysis of forced convective heat transfer coefficients at windward building facades: influence of building geometry. *Journal of Wind Engineering and Industrial Aerodynamics*, *146*, 102–116.

Ng, P. K., Mithraratne, N., & Kua, H. W. (2013). Energy analysis of semi-transparent BIPV in Singapore buildings. *Energy and buildings*, *66*, 274–281.

Nordmann, T., & Clavadetscher, L. (2003). Understanding temperature effects on PV system performance. In *3rd World Conference on Photovoltaic Energy Conversion, 2003. Proceedings of* (pp. 2243–2246). IEEE volume 3.

Norton, B., Eames, P. C., Mallick, T. K., Huang, M. J., McCormack, S. J., Mondol, J. D., & Yohanis, Y. G. (2011). Enhancing the performance of building integrated photovoltaics. *Solar Energy*, *85*, 1629–1664.

Orioli, A., & Di Gangi, A. (2013). A procedure to calculate the five-parameter model of crystalline silicon photovoltaic modules on the basis of the tabular performance data. *Applied energy*, *102*, 1160–1177.

Osseweijer, F. J., Van Den Hurk, L. B., Teunissen, E. J., & van Sark, W. G. (2018). A comparative review of building integrated photovoltaics ecosystems in selected European countries. *Renewable and Sustainable Energy Reviews*, *90*, 1027–1040.

Redweik, P., Catita, C., & Brito, M. (2013). Solar energy potential on roofs and facades in an urban landscape. *Solar Energy*, *97*, 332–341.

Roberts, J. J., Zevallos, A. A. M., & Cassula, A. M. (2017). Assessment of photovoltaic performance models for system simulation. *Renewable and Sustainable Energy Reviews*, *72*, 1104–1123.

Ross, J. (1976). Interface design considerations for terrestrial solar cell modules. In *12th Photovoltaic Specialists Conference* (pp. 801–806).

Saelens, D. (2002). *Energy performance assessment of single storey multiple-skin facades*. Ph.D. thesis KU Leuven.

Saelens, D., & Hens, H. (2001). Experimental evaluation of airflow in naturally ventilated active envelopes. *Journal of Thermal Envelope and Building Science*, *25*, 101–127.

Saelens, D., Roels, S., & Hens, H. (2004). The inlet temperature as a boundary condition for multiple-skin facade modelling. *Energy and Buildings*, *36*, 825–835.

Sánchez-Palencia, P., Martín-Chivelet, N., & Chenlo, F. (2019). Modeling temperature and thermal transmittance of building integrated photovoltaic modules. *Solar Energy*, *184*, 153–161.

Sánchez-Pantoja, N., Vidal, R., & Pastor, M. C. (2018). Aesthetic perception of photovoltaic integration within new proposals for ecological architecture. *Sustainable cities and society*, *39*, 203–214.

Saretta, E., Caputo, P., & Frontini, F. (2018). A review study about energy renovation of building facades with BIPV in urban environment. *Sustainable Cities and Society*, *44*, 343–355.

Silvero, F., Rodrigues, F., Montelpare, S., Spacone, E., & Varum, H. (2018). The path towards Buildings Energy Efficiency in South American Countries. *Sustainable Cities and Society*, *44*, 646–665.

Skoplaki, E., Boudouvis, A., & Palyvos, J. (2008). A simple correlation for the operating temperature of photovoltaic modules of arbitrary mounting. *Solar Energy Materials and Solar Cells*, *92*, 1393–1402.

Skoplaki, E., & Palyvos, J. A. (2009). Operating temperature of photovoltaic modules: A survey of pertinent correlations. *Renewable energy*, *34*, 23–29.

Spiliotis, K., Yordanov, G., Van den Broeck, G., Goverde, H., Baert, K., & Driesen, J. (2017). Towards accurate, high-frequency iv curve measurements of photovoltaic modules applying electronic loads. In *33rd European Photovoltaic Solar Energy Conference and Exhibition* (pp. 1561–1565). WIP; Sylvensteinstrasse 2, D-81369 Munich, Germany.

Sprenger, W., Wilson, H. R., & Kuhn, T. E. (2016). Electricity yield simulation for the building-integrated photovoltaic system installed in the main building roof of the fraunhofer institute for solar energy systems ise. *Solar Energy*, *135*, 633–643.

Swinbank, W. C. (1963). Long-wave radiation from clear skies. *Quarterly Journal of the Royal Meteorological Society*, *89*, 339–348.

Tsai, H.-L. (2010). Insolation-oriented model of photovoltaic module using matlab/simulink. *Solar energy*, *84*, 1318–1326.

Villalva, M. G., Gazoli, J. R., & Ruppert Filho, E. (2009). Comprehensive approach to modeling and simulation of photovoltaic arrays. *IEEE Transactions on power electronics*, *24*, 1198–1208.

Walker, L., Hofer, J., & Schlueter, A. (2019). High-resolution, parametric BIPV and electrical systems modeling and design. *Applied energy*, *238*, 164–179.

Wetter, M. (2004). *Simulation-based building energy optimization*. University of California, Berkeley.

Yang, T., & Athienitis, A. K. (2016). A review of research and developments of building-integrated photovoltaic/thermal (BIPV/t) systems. *Renewable and Sustainable Energy Reviews*, *66*, 886–912.

Zomer, C., & Rüther, R. (2017a). Simplified method for shading-loss analysis in BIPV systems–part 1: Theoretical study. *Energy and Buildings*, *141*, 69–82.

Zomer, C., & Rüther, R. (2017b). Simplified method for shading-loss analysis in BIPV systems. part 2: Application in case studies. *Energy and Buildings*, *141*, 83–95.